



Multidimensional turbulence spectra – Statistical analysis of turbulent vortices [☆]



Farideh Ghasempour ^{*}, Ronnie Andersson, Bengt Andersson

Department of Chemical and Biological Engineering, Chalmers University of Technology, SE-41296 Gothenburg, Sweden

ARTICLE INFO

Article history:

Received 8 July 2013

Received in revised form 26 February 2014

Accepted 6 March 2014

Available online 15 March 2014

Keywords:

Turbulence

Vortex identification algorithm

Vortex properties

Enstrophy

Biot–Savart law

LES

ABSTRACT

Strong nonlinear or very fast phenomena such as mixing, coalescence and breakup in chemical engineering processes, are not correctly described using average turbulence properties. Since these phenomena are modeled by the interaction of fluid particles with single or paired vortices, distribution of the properties of individual turbulent vortices should be studied and understood. In this paper, statistical analysis of turbulent vortices was performed using a novel vortex tracking algorithm. The vortices were identified using the normalized Q-criterion with extended volumes calculated using the Biot–Savart law in order to capture most of the coherent structure related to each vortex. This new and fast algorithm makes it possible to estimate the volume of all resolved vortices. Turbulence was modeled using large-eddy simulation with the dynamic Smagorinsky–Lilly subgrid scale model for different Reynolds numbers. Number density of turbulent vortices were quantified and compared with different models. It is concluded that the calculated number densities for vortices in the inertial subrange and also for the larger scales are in very good agreement with the models proposed by Batchelor and Martinez-Bazán. Moreover, the associated enstrophy within the same size of coherent structures is quantified and its distribution is compared to models for distribution of turbulent kinetic energy. The associated enstrophy within the same size of coherent structures has a wide distribution that is normal distributed in the logarithmic scale.

© 2014 The Authors. Published by Elsevier Inc. This is an open access article under the CC BY-NC-ND license (<http://creativecommons.org/licenses/by-nc-nd/3.0/>).

1. Introduction

A detailed description of turbulence spectra is needed to model and quantify many aspects of engineering flows e.g. the behavior of turbulent mixing, coalescence and break-up phenomena in chemical engineering processes [1]. One of the main mechanisms behind these phenomena is the interaction of fluid particles with single or paired turbulent vortices. The aforementioned phenomena usually occur very fast, often within a few milliseconds [2], and this time scale is equal to or smaller than the life time of turbulent vortices for many engineering applications [3]. Thus, the interaction cannot be modeled using the statistical mean properties of turbulence e.g. turbulent kinetic energy and dissipation rate [3–5]. Instead, the interaction might be better described by the distribution of the properties of single turbulent vortices, such as vortex size, lifetime, number density (the number of turbulent vortices per unit fluid volume), growth and dissipation rate, and the turbulent kinetic energy for vortices of different sizes at different locations.

[☆] This article belongs to the Special Issue: *Topical Issues drawn from CFD2012 on CFD in the Minerals and Process Industries.*

^{*} Corresponding author. Tel.: +46 31 7722982.

E-mail address: farideh@chalmers.se (F. Ghasempour).

Nomenclature

C	structure function parameter (-)
C_s	Smagorinsky constant (-)
E	turbulent energy spectrum ($\text{m}^3 \text{s}^{-2}$)
L	largest turbulent vortices length scale and pipe length (m)
\dot{n}	number density (m^{-3})
Q	Q-criterion (s^{-2})
r	distance (m)
R	radius (m)
Re_λ	Taylor microscale Reynolds number
S	strain rate (s^{-1})
t	time (s)
u	fluctuating velocity (m s^{-1})
\bar{u}	mean of fluctuating velocity (m s^{-1})
x, y, z	coordinates
y^+	wall unit (-)

Greek letters

Δ	turbulence resolution filter size (m)
\emptyset	pipe diameter (m)
α	Kolmogorov constant (-)
ε	energy dissipation rate ($\text{m}^2 \text{s}^{-3}$)
κ	wave number (m^{-1})
λ	vortex size (m)
λ_2	eigenvalue of velocity gradient tensor
ν	kinematic viscosity ($\text{m}^2 \text{s}^{-1}$)
ρ	density (kg m^{-3})
τ	vortex turnover time (s)
ω	vorticity (s^{-1})

Superscripts and subscripts

<i>ind.</i>	induced velocity in Biot–Savart integral
<i>n</i>	normalized
<i>T</i>	residual part in LES grid filter

Acronyms

LES	large eddy simulation
RANS	Reynolds-averaged Navier–Stokes
TKE	turbulent kinetic energy
SGS	subgrid scale
Ens	enstrophy

Moreover the detailed description of turbulence spectra helps to improve understanding of turbulence. The understanding of turbulence is a part of “wish list” suggested at Turbulence Colloquium in Marseille 2011 for current and future studies [6]. The intention of this research work is to improve the understanding of turbulence. For this purpose, a vortex-identification algorithm that allows the details of the single turbulent vortices to be visualized and their properties to be quantified, is required. Several vortex-identification algorithms are proposed in the literature. Many of the vortex identification algorithms identify the important regions include vortex cores, critical points for vector fields and regions that fit into predefined ideal shapes; but little work has been done to identify the real shape of three dimensional individual turbulent flow structures so far. In addition, there is still a need for developing novel methodologies that improve the study of three-dimensional turbulent structures’ properties.

Among the turbulent vortex properties, the vortex number density is critical for modeling of coalescence and break-up processes. Existing models predict different vortex number densities and they are only valid for the inertial subrange of the energy spectrum of turbulent flows. No model is available which is valid for a wider range of flow situations [7,8]. In addition the vortex number distributions should be used to derive expressions relating to the fractional rate of surface renewal and mass transfer coefficients across gas–liquid and solid–liquid interfaces [9]. For these reasons, a systematic evaluation of available models on vortex number density is required as a foundation for further investigations.

The objective of the present study is to perform statistical analyses of turbulent vortices identified by a novel vortex-identification algorithm developed by the authors. The vortex-identification algorithm was developed to visualize and identify all individual turbulent vortices resolved by LES, and quantify their turbulent properties. The turbulent vortex core was extended by computing the induced-velocities based on the Biot–Savart law in order to capture more of the coherent structure that is related to the vortex core. The calculated number density of turbulent vortices is compared with predicted number densities from existing models. The properties of the vortices including enstrophy and vortex size are described as function of radial position at two different flow conditions.

2. Computational details

2.1. Modeling of vortex number density

Generally, number density of turbulent vortices, \dot{n} , is defined as the number of turbulent vortices per unit fluid volume. A relationship between the number density of turbulent vortices of sizes between λ and $\lambda + d\lambda$ and turbulent energy spectrum, $E(\kappa)$, can be formulated by writing an energy balance for vortices of wave number between κ and $\kappa + d\kappa$ in the inertial subrange

$$\dot{n}_\lambda \rho_c \frac{\pi}{6} \lambda^3 \frac{\bar{u}_\lambda^2}{2} d\lambda = E(\kappa) \rho_c (-d\kappa). \quad (1)$$

Here, the wave number, κ , is $2\pi/\lambda$. \bar{u}_λ is the mean fluctuating velocity of turbulent vortices of size λ and it is theoretically given by [10],

$$\bar{u}_\lambda \approx C^{1/2} (\varepsilon \lambda)^{1/3}, \quad (2)$$

where C is the functional parameter of the turbulent structure. A number of authors reported different estimates for C as shown in Table 1.

The turbulent energy spectrum in the inertial subrange is

$$E(\kappa) = \alpha \varepsilon^{2/3} \kappa^{-5/3}. \quad (3)$$

On substituting of Eqs. (2) and (3) into Eq. (1) the number density of turbulent vortices of sizes between λ and $\lambda + d\lambda$ is given by

$$\dot{n}_\lambda = \frac{C_1}{\lambda^4}, \quad (4)$$

and

$$C_1 = \frac{24\alpha}{(2\pi)^{5/3} C}. \quad (5)$$

The experimental data shows that the constant α is 1.5 approximately [11]. According to Table 1, and applying the values for the coefficient C , a variety of coefficient C_1 in the number density equation can be found. Different values for the coefficient C_1 are summarized in Table 1.

Risso and Fabre [12] have used the same value as given by Pope [13] and Lasheras [14] has pointed out that there is a range for C from about 2–8.2. In this study, several number density models for turbulent vortices suggested in the literature were applied and compared with the number density of turbulent vortices quantified by using the vortex tracking algorithm.

2.2. Large eddy simulation and assessment

In this work, turbulence was modeled using large eddy simulation (LES) with the dynamic Smagorinsky–Lilly subgrid scale model. In LES the governing equations, continuity and momentum equations, are separated into resolved and subgrid parts by a spatial filtering operation. The governing equations with an added subgrid stress tensor are:

Table 1

Various coefficients in the number density models in the literature.

Model	C	C_1
Jakobsen [10]	2	0.841
Luo and Svendsen [5]	2.045	0.822
Batchelor [15]	7.23	0.2327
Pope [13]	1.973	0.8528
Martinez [26]	8.2	0.2052

$$\frac{\partial \bar{u}_i}{\partial x_i} = 0, \tag{6}$$

$$\frac{\partial \bar{u}_i}{\partial t} + \frac{\partial}{\partial x_j} (\bar{u}_i \bar{u}_j) = -\frac{1}{\rho} \frac{\partial \bar{p}}{\partial x_j} + 2\nu \frac{\partial}{\partial x_j} (\bar{S}_{ij}) - \frac{\partial \tau_{ij}}{\partial x_j}, \tag{7}$$

where τ_{ij} is the subgrid stress tensor and $\bar{S}_{ij} = \frac{1}{2} (\frac{\partial \bar{u}_i}{\partial x_j} + \frac{\partial \bar{u}_j}{\partial x_i})$ represents the resolved strain rate tensor. The Smagorinsky model is:

$$\tau_{ij} - \frac{1}{3} \tau_{kk} \delta_{ij} = -2\nu_T \bar{S}_{ij}. \tag{8}$$

Regarding ν_T , which represents the subgrid turbulent eddy viscosity, Smagorinsky proposed the first subgrid scale model (SGS) entitled the Smagorinsky–Lilly SGS.

$$\nu_T = (C_S \Delta_g)^2 |\bar{S}|. \tag{9}$$

Here Δ_g is the filter size and $|\bar{S}| = (2\bar{S}_{ij}\bar{S}_{ij})^{1/2}$ is magnitude of the resolved strain rate. The coefficient C_S is determined using the dynamic model [13].

Most equipment in chemical process industries are run at low Reynolds numbers, and Reynolds numbers of 20,000 and 50,000 were selected as suitable ones for this study. The simulations were performed for a turbulent pipe flow ($\varnothing = 5$ cm, $L = 20$ cm) of water at these Reynolds numbers. The corresponding Taylor microscale Reynolds numbers, shown in Table 2, indicate a very narrow inertial subrange.

The length of the pipe was selected to obtain an average residence time, in the same order as the expected life time of the large energy containing turbulent vortices. Periodic boundary conditions were used in the axial direction. The two grid resolutions, one for each Reynolds number, allowed most of the turbulent kinetic energy in the inertial subrange to be resolved and the largest grid dimension was 0.5 mm in axial direction and less in radial direction. The mean Taylor microscale sizes, estimated from RANS simulation of the same flow conditions, were approximately 6 to 4 mesh sizes.

In the LES simulations, for space discretization, the bounded central differencing and for time discretization the second order implicit algorithms were used. The numerical procedure was based on an implicit iterative technique with a pressure based solver. It is important that the LES simulations are run for at least a few mean flow residence times to become statistically steady [16]. The statistically steadiness was checked by monitoring the time averaged and the turbulent properties at different points inside the computational domain. Data sampling for turbulence statistics started after about 10 residence times.

The quality of the LES simulations were assessed in terms of the ratio of the resolved turbulent kinetic energy to the total turbulent kinetic energy, the ratio of SGS turbulent viscosity to the molecular viscosity, two-point correlations of velocities and the y^+ value for the different Reynolds numbers. In addition, a mesh convergence study was carried out for two different mesh resolutions in order to assure the quality of the LES simulations.

As shown in Fig. 1, the ratio of the resolved turbulent kinetic energy to the total for the two Reynolds numbers studied, showed that more than 90% of the total turbulent kinetic energy in the bulk of the flow and more than 80% at $y^+ > 5$ was captured. When 80% of the turbulent kinetic energy is resolved, the LES simulation can be considered well-resolved [17].

Another measure of resolution quality is the ratio of instantaneous subgrid turbulent viscosity to the molecular viscosity. In these LES simulations the instantaneous subgrid turbulent viscosity ratio was lower than 0.1 at $y^+ < 5$, and the maximum of this ratio in the bulk of the flow was 1.55. Furthermore, the maximum instantaneous and average wall y^+ were 1.7 and 0.85, respectively, which are in the accepted region for LES simulation. Fig. 2 shows the power spectra in axial direction at the center of the pipe for $Re = 20,000$. An inertial sub-range is obtained for $\kappa < 1000$ or $L_{11} = 2\pi/\kappa > 6$ mm. The vortices are stretched in the streamline direction with an aspect ratio in the range 3–5 [18]. Consequently, the equivalent sphere diameter with the same volume will be around 2–3 mm and we conclude that the lower range for the inertial subrange is 2 mm at $Re = 20,000$.

Two-point correlations of velocities, is another important method to determine the resolution of resolved-scale flow field in large eddy simulation. Su et al. [19] and Davidson [20] used two point correlations of velocities to quantify how many cells

Table 2
Properties of flow and turbulence for both Reynolds numbers.

	Re = 20,000	Re = 50,000
Mean Taylor microscale Re_λ	80	101
Residence time (s)	0.5	0.2
Mean vortex life time, $\tau_{L-mean} = k/\epsilon$ (s)	0.57	0.21
Estimated lower range of inertial sub range (mm)	2	1.5

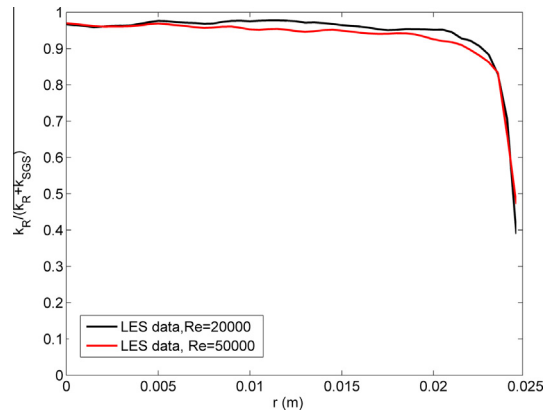


Fig. 1. Ratio of the resolved turbulent kinetic energy to the total turbulent kinetic energy for the two different Reynolds numbers. k_R is the resolved turbulent energy.

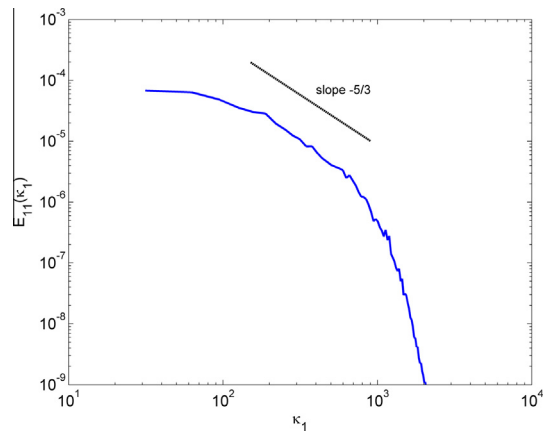


Fig. 2. Energy spectrum in axial direction for $Re = 20,000$.

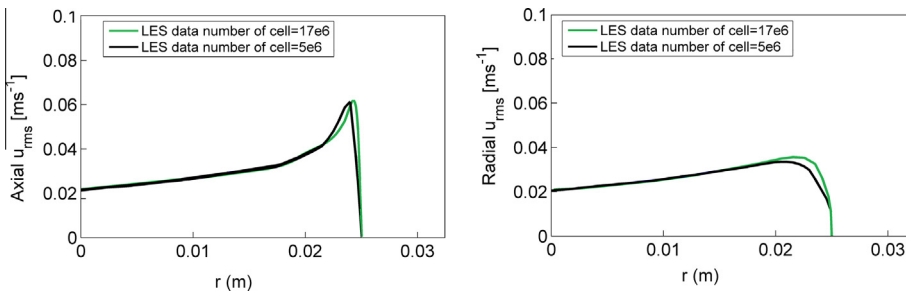


Fig. 3. The axial and radial root-mean-squared velocities of the LES data for Reynolds number 20,000 and two different mesh resolutions.

are resolving the large structures. At least five to ten cells are required to ensure that the largest scales are well resolved in LES [20]. For both Reynolds numbers studied, the two-point correlation analysis showed that at least fifteen grid cells were resolving the large scales.

The mesh convergence study showed that the LES simulations were almost mesh independent. Fig. 3 shows the variations of axial and radial root-mean-squared velocities of the LES data for Reynolds number 20,000, as function of the radial location, for two different mesh resolutions. The difference is minor and the RMS is somewhat higher close to the wall as expected since a larger part of the turbulent kinetic energy is resolved with finer mesh. Similar results were obtained for the Reynolds number of 50000.

3. Vortex identification and analysis methods

Several Eulerian methods for flow structure visualization are proposed in the literature. They are generally formulated in terms of the invariants of the velocity gradient tensor. These criteria includes the iso-surfaces of vorticity, stream lines, Helicity, Q-criterion, complex eigenvalues of the velocity gradient tensor, λ_2 , swirl strength and pressure minimum [21]. Chakraborty and et al. [22] showed that the Q-criterion and λ_2 almost give the same flow structures.

When there is no imposed non-uniform strain field in the turbulent flow, the Q-criterion can be used to identify the core location of the turbulent vortices. The Q-criterion represents the local balance between vorticity and strain rate. In order to visualize a wide range of vortices even the weakest one in the bulk, the Q-criterion can be normalized with respect to the vorticity [18].

In this study, a vortex-identification algorithm was developed in order to visualize and identify the 3D turbulent vortices. As shown in Fig. 4, the proposed vortex-identification algorithm contains four steps.

In the first step, a 3D image segmentation algorithm was used to visualize and identify the core of individual vortices. In the algorithm, turbulent vortices were visualized by iso surfaces of normalized Q-criterion. Theoretically, positive values of the normalized Q-criterion represent vortices; however in this study, the normalized Q-criterion larger than 0.1 was used as a cut off, in order to have a clear separation between vortices. This cut off provides a good balance that captures the core of the turbulent vortices but excludes most of the incoherent turbulent flow.

In a binary image space the volume was identified as inside or outside the boundary described by the normalized Q-criterion. By using the “bwconncomp” function in MATLAB, the connected regions were identified and labeled with unique numbers. The properties within each labeled connected region can be integrated over the volume of the region to obtain the corresponding turbulent vortex data. Furthermore, the total number of identified regions provided the total number of turbulent vortices. Therefore by using the algorithm, the cores of the turbulent structures visualized by normalized Q-criterion can be identified and indexed through the entire computational domain at each time. This methodology also helps to correlate size of the vortices to other properties e.g. location and enstrophy. In this study, for all labeled turbulent vortices data such as volume, location and enstrophy were quantified.

Recently, an analysis of the turbulent kinetic energy on a 2D plane of a 3D LES simulation revealed that less than 40% of the turbulent kinetic energy (TKE) on the plane would be captured within the structures identified by the lowest possible cut off Q-criterion [18]. This occurs because the Q-criterion represents just the vortex cores even with the lowest possible cut off criterion. Fig. 5 shows that the normalized Q-criterion captures only the core of turbulent vortices while the most of turbulent kinetic energy is located outside of them. Enstrophy is well captured within the vortex cores described by the normalized Q-criterion, by excluding the near wall area at $y^+ < 30$ more than 60% of the enstrophy is within the vortex cores.

Since turbulent kinetic energy (TKE) is one of the key parameters in the breakage, coalescence and mixing phenomena, it was of interest to quantify the amount of TKE in the coherent structures identified with this algorithm. Fig. 6 shows the

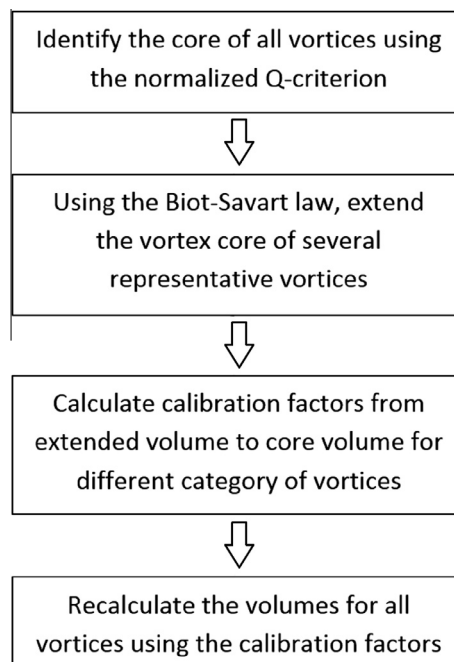


Fig. 4. The four steps of the proposed vortex-identification algorithm.

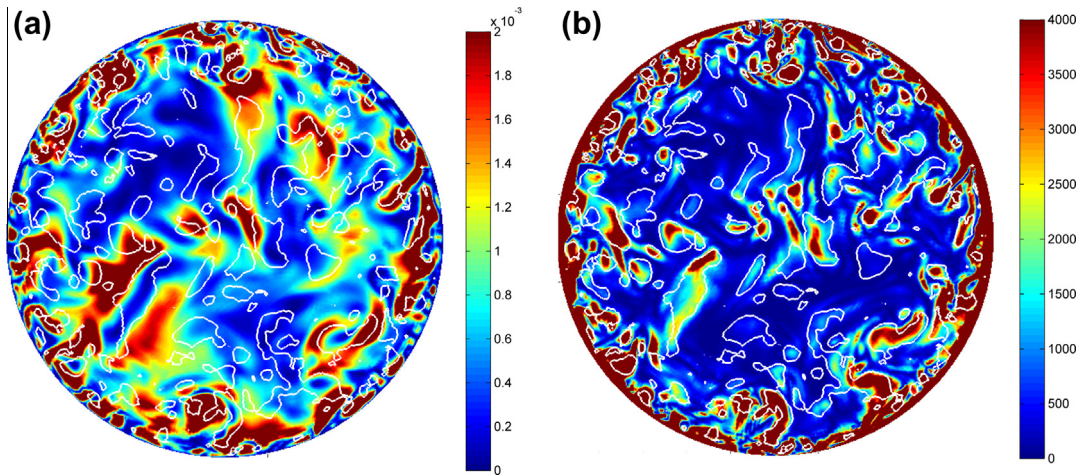


Fig. 5. (a) Overlap of turbulent kinetic energy, $0 < \text{TKE} < 0.002 \text{ [m}^2/\text{s}^2]$ and turbulent structures identified using iso-normalized Q-criterion > 0.1 ; (b) overlap of enstrophy, $0 < \text{Ens} < 4000 \text{ [1/s}^2]$ and turbulent structures identified using iso-normalized Q-criterion > 0.1 .

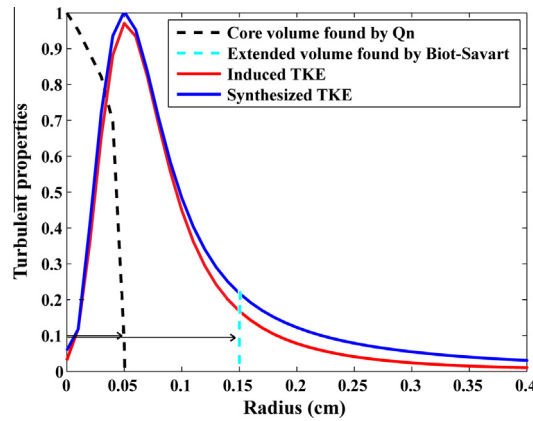


Fig. 6. Turbulent kinetic energy distribution in an idealized Lamb–Oseen vortex.

distribution of turbulent kinetic energy for an idealized Lamb–Oseen vortex. Since the cut off used in the algorithm (0.1) is located very close to the peak in turbulent kinetic energy (Fig. 6), an extension of the volume identified with the normalized Q-criterion will allow more turbulent kinetic energy to be captured within the vortex. To extend the vortex volume, the Biot–Savart law was implemented.

A distribution of vorticity in a vortex induces the relative velocity field based on the Biot–Savart law [23]. According to the Helmholtz–Hodge decomposition, any smooth vector field which decays sufficiently fast to infinity may be uniquely determined by its curl and divergence, and can be written as the sum of a curl (solenoid or divergence free) and a divergence (irrotational). The irrotational part can be described using potential flow and the curl part can be calculated by the Biot–Savart law. The induced-velocity generated by Biot–Savart law in a three dimensional volume can be expressed as:

$$u_{ind.} = \frac{1}{4\pi} \int_V \omega \times \nabla \left(\frac{1}{r} \right) dV = \frac{1}{4\pi} \int_V \left\{ \frac{1}{r} (\nabla \times \omega) - \nabla \times \left(\frac{1}{r} \omega \right) \right\} dV. \tag{10}$$

Here $u_{ind.}$, ω , r and V are induced velocity, vorticity, distance between points and volume of the vortex cores respectively.

By applying the Biot–Savart law in three-dimensions to generate the induced-velocities of the vortex, the volume of the vortex can be extended in order to cover the peak in the turbulent kinetic energy which is obtained from the induced velocities (Fig. 6). This extended volumes allows more TKE to be confined within the extended vortex, while the extended vortex keeps the shape of the core-vortex.

In this study, the Biot–Savart law in three-dimensions was firstly tested on a Lamb–Oseen vortex synthesized with specific parameters. Fig. 6 shows the Lamb–Oseen vortex radius estimated by the normalized Q-criterion and the one extended based on the Biot–Savart law. The vortex volume extension was based on capturing 85% of the total turbulent

kinetic energy, which was calculated from the induced velocities, within the vortex. The figure shows the turbulent kinetic energy calculated from the synthesized idealized Lamb–Oseen vortex and the induced velocities using Eq. (10). As shown in Fig. 6 the distribution of the induced-velocities using Biot–Savart were very similar to the synthesized velocities. Only the core of the vortex captured by the normalized Q-criterion was used in the integration of Eq. (10) to induce the velocities.

For a vortex, the axial length of the turbulent structure can be captured with the normalized Q-criterion while the radial size will be underestimated. Fig. 6 shows that the radius of the core-vortex idealized Lamb–Oseen vortex must be much larger to capture 85% of the total induced turbulent kinetic energy. However, an appropriate extension criterion cannot be determined from idealized Lamb–Oseen vortex data, since real vortices are affected by neighboring vortices and the energy dissipation in the fluid. Instead, the extension criterion was obtained by analyzing the LES data using the Biot–Savart law to extend the volume from the core region determined with the normalized Q-criterion. The objective was that 85% of the turbulent kinetic energy associated with the vortex should be captured, and the induced turbulent kinetic energy was calculated from the Biot–Savart calculation (Eq. (10)) based on the vorticity of the core-vortex. The iso-surface was obtained from connecting the points around an iso-Q surface where the induced velocities calculated from Biot–Savart decreased to 40% of its maximum value. This results in capturing close to 85% of the total TKE. Fig. 7a shows the iso surface of a sample vortex visualized by iso normalized Q-criterion. The iso surface of the extended vortex based on its induced velocity using the Biot–Savart law was shown in Fig. 7b. This extended vortex contains the maximum peak region of the total induced turbulent kinetic energy within the extended volume. Fig. 7c shows the top view of these two iso surfaces overlapped.

Fig. 8 shows the ratio of the extended volume based on the Biot–Savart law to the core volume obtained from the iso normalized Q-criterion for a number of vortices in the LES data. The ratio was different for various vortex sizes. Particularly for the smallest vortices, there were large differences in their ratios. The reason is that these vortices were located in different areas; the smallest vortices were mostly located in an area close to the wall and most of the turbulent kinetic energy variation occurs in that area. The average ratio was computed over three different size groups based on their equivalent diameters (equivalent spheres). As shown in Fig. 8, the average ratio of the extended volume based on the Biot–Savart law with respect to the core volume obtained from the iso normalized Q-criterion was varying between 2.25 and 1.75, and the corresponding standard deviations between 0.6 and 0.2.

The Biot–Savart calculation takes a great deal of time to process for all vortices. Consequently it was not possible to analyze thousands of vortices, identified through the entire of the computational domain, based on their Biot–Savart calculations separately. Instead, to simplify the statistical analysis of turbulence, all core volumes identified by the vortex tracking algorithm were multiplied by the average ratios of the extended to the core volume to get closer to the aimed conditions. More specifically, the volumes of vortices which their equivalent diameters were less than 1 mm were multiplied by 2.25 and the ones which their equivalent diameters were between 1 and 2 mm were multiplied by 2 and for the rest of core volumes a factor equal to 1.75 was applied. Subsequently, the diameters of equivalent spheres were calculated from the extended volumes. Using this average extension of the core volume will introduce some error but even for the vortices below 1 mm the ratio in volume is within 1.5 and 3 for more than 90% of the vortices. This difference corresponds to an error of less than 15% in estimated diameter using the constant value 2.25.

Since the turbulent kinetic energy and number of turbulent vortices are varying with the pipe radius and most of the variations are in areas with high shear rate close to the wall, it was highly motivated to do the statistical analysis also at different radial locations. In this study, the analysis was done for 5 radial fractions. Data sampling and statistical analysis were further performed at three different axial pipe segments. Three six-centimeter axial pipe segments were considered. Since we do not expect any axial difference in turbulent statistics, this separation will show the stability of the vortex tracking algorithm.

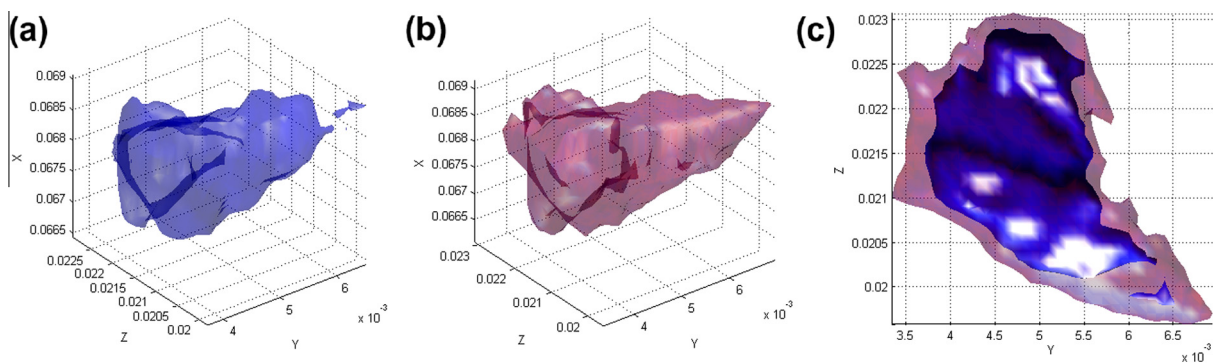


Fig. 7. (a) Iso surface of normalized Q-criterion; (b) the iso surface of the extended vortex based on its induced velocity using the Biot–Savart law; (c) a cross section of the superimposed volumes.

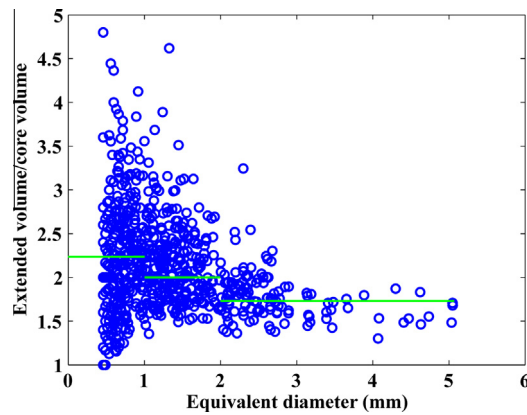


Fig. 8. Ratio of extended volume found using Biot–Savart to the original. The green lines show the average of the ratio for different range of equivalent diameter. (For interpretation of the references to color in this figure legend, the reader is referred to the web version of this article.)

4. Results and discussion

In this study, the turbulence properties such as vortex number density, enstrophy distribution, volume (core and the extended volume) and location were computed and analyzed by using the vortex identification algorithm. The vortex-identification algorithm was implemented to LES simulation of a turbulent pipe for two different Reynolds numbers, 20,000 and 50,000. More than 8100 and 13,300 vortex cores were identified at these two flow conditions respectively.

4.1. Number density models for turbulent vortices

The number density of turbulent vortices was calculated using relevant literature models (Table 1), and compared with the results obtained with the vortex tracking algorithm. In fact, the number density of turbulent vortices of various models was calculated for vortex sizes between λ and $\lambda + d\lambda$. In this work, the bin sizes were small for the smaller vortices and increasing gradually for the larger ones.

The number density of turbulent vortices at three different axial segments of pipe (Initial, Middle and End) had the same distribution which confirms the stability of the vortex tracking algorithm. However, for the largest vortices, the number densities deviate slightly, mainly due to the fact that a low number of large vortices were identified.

In Fig. 9, the number density of turbulent vortices quantified by means of the vortex tracking algorithm are compared with the number densities of turbulent vortices computed by using the models in Table 1. Since all these models are valid only in the inertial subrange, the number densities of turbulent vortices predicted by the models are plotted only for the inertial subrange in Fig. 9.

The comparison shows that the number density of turbulent vortices quantified by means of the vortex tracking algorithm has similar size dependence as the models. In particular the number densities computed from the Batchelor

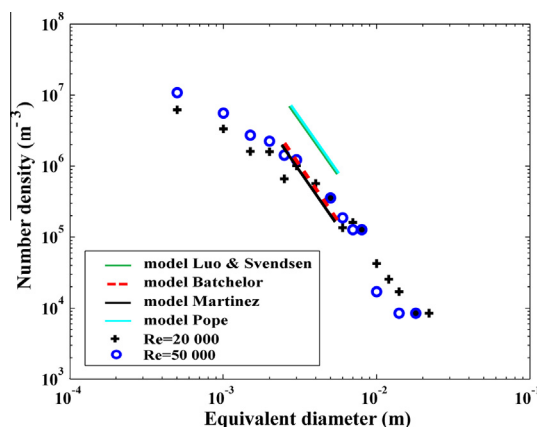


Fig. 9. Comparison between number densities identified with the vortex tracking algorithm and the different models. (The models by Pope and Lou and Svendsen coincide in the figure).

and Martinez-Bazán models agree very well for vortex sizes in the inertial subrange. Since the values of constant C (Table 1) obtained by Batchelor and Martinez-Bazán are so close, the results obtained by their models are the same. The other models predicted almost three times higher number density.

Below the inertial subrange all the models over predict the number density. This is expected since the smallest vortices are not resolved with our mesh size and the dissipation of turbulent kinetic energy affects the small turbulent scales. For larger vortices there was a considerable compatibility between the number densities of turbulent vortices quantified and modeled specially the number densities computed with the Batchelor and Martinez-Bazán models. Therefore the rest of analysis was performed by using the Batchelor and Martinez-Bazán models.

By increasing the Reynolds number, the inertial subrange in a turbulent flow is increased [24]. As shown in Fig. 9, the range over which the number densities are following the modeled line, is larger in the case of higher Reynolds number i.e. at Re = 50,000, which is expected.

Showing the number densities of all vortices independent of their locations as in Fig. 9 may be misleading since the average number of vortices will be dominated by more vortices in the near wall region. The number density of turbulent vortices is shown as a function of the radial position in Fig. 10. As shown here the number density of turbulent vortices calculated with the Batchelor model, agrees somewhat better near the pipe wall ($0.8 < r/R < 1$) than in the core of the pipe.

4.2. Enstrophy of turbulent vortices

Moreover, the vortex tracking algorithm revealed details of the vortex properties including enstrophy distribution. An analysis of the associated enstrophy within the turbulent coherent structures found by the normalized Q-criterion showed that the enstrophy is increasing with the radial position in the pipe. The accumulated probability distribution of the volume averaged enstrophy of each vortex is shown as a function of five radial locations in Fig. 11.

The volume averaged enstrophy distribution of vortices was expected to be analogous to the distribution of turbulent kinetic energy. The fluctuating velocity at the surface of the iso-Q volume can be approximated by $u \propto \omega R$ and the turbulent kinetic energy which is the square of the fluctuating velocity can be correlated with the enstrophy by $k \propto \omega^2 R^2$. Therefore, the enstrophy for each vortex size should have the similar probability distribution as turbulent kinetic energy in the inertial subrange.

It is frequently assumed that for each vortex size, λ , there is a distribution of fluctuating velocities. A model of turbulent kinetic energy probability distribution, $p_e(\varphi)$, is given by Angelidou et al. [25],

$$p_e(\varphi) = \frac{1}{\bar{e}(\lambda)} \exp(-\varphi), \tag{11}$$

where

$$\varphi = \frac{e(\lambda)}{\bar{e}(\lambda)}. \tag{12}$$

Here $\bar{e}(\lambda)$ is the average vortex energy in the inertial subrange for a vortex size λ .

The cumulative distribution of volume averaged enstrophy for all vortex sizes grouped together vs. the logarithm of normalized enstrophy is shown in Fig. 12. The volume averaged enstrophy was normalized by the average vortex enstrophy for each vortex size λ . The blue and red curves are for Reynolds numbers 20,000 and 50,000, respectively. The distributions are normal distributed in the logarithm scale as seen by the circle and diamond legends on top on the blue and red curves that shows the cumulative normal distribution. The cumulative distribution of Eq. (11) is shown as the black line in Fig. 12. It can

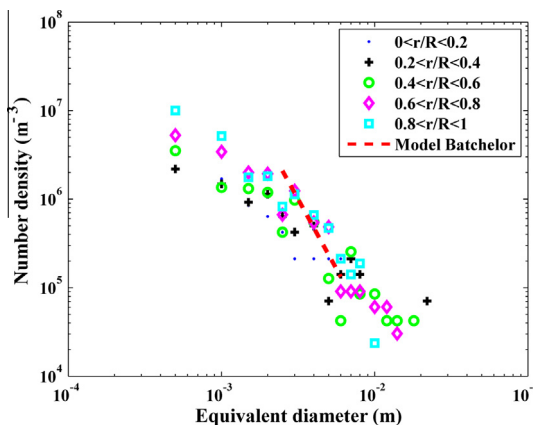


Fig. 10. Number density of turbulent vortices at different radial locations.

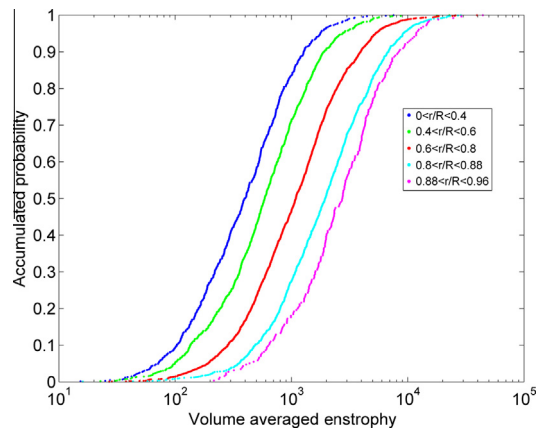


Fig. 11. Volume averaged enstrophy of turbulent vortices at different radial locations.

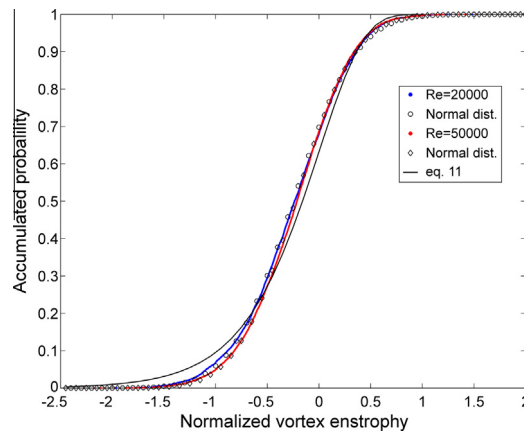


Fig. 12. The probability distribution of weighted enstrophy comparing with normal and exponential distributions.

be concluded that the zero parameter model by Angelidou et al. [25] predicts a reasonable but not perfect distribution of enstrophy.

5. Conclusions

The study was done at rather low Reynolds numbers 20,000 and 50,000, corresponding to Taylor microscale Reynolds numbers 80 and 101, respectively. At these low Reynolds numbers the inertial subrange is very narrow. However, these flow conditions are close to what is observed in chemical process equipment and motivates a detailed study.

The LES simulations were done with very good resolution. Two point correlation analyses showed that at least fifteen grid cells were resolving the large scales. Also more than 95% of the total turbulent kinetic energy was resolved and the maximum subgrid turbulent viscosity to molecular viscosity ratio was 1.55.

An efficient vortex tracking algorithm that allows identification of thousands of vortices, and quantification of turbulent properties, needed for statistical analysis of turbulence was developed.

It was shown that by using the Biot–Savart law in three-dimensions the core size of a vortex estimated by the normalized Q -criterion can be extended to the larger size to increase the amount of turbulent kinetic energy captured within the vortex. However, the extending volumes based on Biot–Savart law may conflict with the requirement of a clear separation between the vortices, which is necessary when vortices are tracked over time.

A separate analysis of the coherent vortices in three different axial segments of the pipe gave almost identical results, confirming the stability of the algorithm; only a random effect was noticed mainly due to the identification of very low numbers of the largest vortices.

The calculated number densities of vortices in the inertial subrange and larger scales agree very well with the Batchelor and Martinez-Bazán models in the literature. There is some difference in radial position for the larger vortices but no valid conclusions can be drawn since there are too few vortices in each bin size for large vortices. The effect of Reynolds number on

vortex number density distribution is minor with a tendency to decrease the slope of the distribution at lower Reynolds number. This is due to a more narrow inertial subrange at low Reynolds number. However determining the exact region of inertial subrange is challenging since it is a local value and depends on local dissipation rates.

The enstrophy distribution for a given vortex size is very large and this variation must be taken into account when estimating properties of turbulent flow e.g. for calculation of break-up rate of bubbles and drops. The associated enstrophy within the same size of coherent structures is normal distributed in the logarithmic scale.

References

- [1] S.S. Deshpande, M.V. Tabib, J.B. Joshi, V.R. Kumar, B.D. Kulkarni, Analysis of flow structures and energy spectra in chemical process equipment, *J. Turbul.* 11 (2010) 1–39.
- [2] R. Andersson, B. Andersson, On the breakup of fluid particles in turbulent flows, *AIChE J.* 52 (2006) 2020–2030.
- [3] R. Andersson, B. Andersson, F. Chopard, T. Noren, Development of a multi-scale simulation method for design of novel multiphase reactors, *Chem. Eng. Sci.* 59 (2004) 4911–4917.
- [4] R. Andersson, B. Andersson, Modeling the breakup of fluid particles in turbulent flows, *AIChE J.* 52 (2006) 2031–2038.
- [5] H. Luo, H.F. Svendsen, Theoretical model for drop and bubble breakup in turbulent dispersions, *AIChE J.* 42 (1996) 1225–1233.
- [6] Marseille, *Turbulence Colloquium Marseille 2011*, in, 2011.
- [7] Y.X. Liao, D. Lucas, A literature review of theoretical models for drop and bubble breakup in turbulent dispersions, *Chem. Eng. Sci.* 64 (2009) 3389–3406.
- [8] Y.X. Liao, D. Lucas, A literature review on mechanisms and models for the coalescence process of fluid particles, *Chem. Eng. Sci.* 65 (2010) 2851–2864.
- [9] Z.B. Zhang, C.R. Thomas, Eddy number distribution in isotropic turbulence and its application for estimating mass transfer coefficients, *Chem. Eng. Commun.* 140 (1996) 207–217.
- [10] H.A. Jakobsen, *Chemical Reactor Modeling – Multiphase Reactive Flows*, Springer, 2008.
- [11] H. Tennekes, J.L. Lumley, *A First Course in Turbulence*, MIT Press, 1972.
- [12] F. Risso, J. Fabre, Oscillations and breakup of a bubble immersed in a turbulent field, *J. Fluid Mech.* 372 (1998) 323–355.
- [13] S.B. Pope, *Turbulent Flows*, Cambridge University Press, Cambridge, 2000.
- [14] J.C. Lasheras, C. Eastwood, C. Martínez-Bazán, J.L. Montañés, A review of statistical models for the break-up of an immiscible fluid immersed into a fully developed turbulent flow, *Int. J. Multiphase Flow* 28 (2002) 247–278.
- [15] G.K. Batchelor, *The Theory of Homogeneous Turbulence*, Cambridge University Press, Cambridge, 1982.
- [16] J. Jimenez, A.A. Wray, P. Saffman, R.S. Rogallo, The structure of intense vorticity in isotropic turbulence, *J. Fluid Mech.* 225 (1993).
- [17] S.B. Pope, Ten questions concerning the large-eddy simulation of turbulent flows, *New J. Phys.* 6 (2004).
- [18] F. Ghasempour, R. Andersson, N. Kevlahan, B. Andersson, Multidimensional turbulence spectra – identifying properties of turbulent structures, *J. Phys: Conf. Ser.* 318 (2011) 042022.
- [19] H.B. Su, R.H. Shaw, U. Paw, Two-point correlation analysis of neutrally stratified flow within and above a forest from large-eddy simulation, *Boundary-Layer Meteorol.* 94 (2000) 423–460.
- [20] L. Davidson, Large eddy simulations: how to evaluate resolution, *Int. J. Heat Fluid Flow* 30 (2009) 1016–1025.
- [21] J. Jeong, F. Hussain, On the identification of a vortex, *J. Fluid Mech.* 285 (1995) 69–94.
- [22] P. Chakraborty, S. Balachandar, R.J. Adrian, On the relationships between local vortex identification schemes, *J. Fluid Mech.* 535 (2005) 189–214.
- [23] P.A. Davidson, *Turbulence – An Introduction for Scientists and Engineers*, Oxford University Press, United Kingdom, 2004.
- [24] B. Andersson, R. Andersson, L. Håkansson, M. Mortensen, R. Sudiyo, B. Wachem, *Computational Fluid Dynamics for Engineers*, Cambridge University Press, Cambridge, 2012.
- [25] C. Angelidou, M. Psimopoulos, G.J. Jameson, Size distribution functions of dispersions, *Chem. Eng. Sci.* 34 (1979) 671–676.
- [26] C. Martínez-Bazán, J.L. Montañés, J.C. Lasheras, On the breakup of an air bubble injected into a fully developed turbulent flow. Part 2 size PDF of the resulting daughter bubbles, *J. Fluid Mech.* 401 (1999) 183–207.